Powder Technology 351 (2019) 54–65

Contents lists available at ScienceDirect

Powder Technology

journal homepage: www.elsevier.com/locate/powtec

Modeling the effective conductivity of the solid and the pore phase in granular materials using resistor networks

Oleg Birkholz [a,*], Yixiang Gan [b], Marc Kamlah [a]

[a] Karlsruhe Institute of Technology, Hermann-von-Helmholtz-Platz 1, 76344 Eggenstein-Leopoldshafen, Germany
[b] The School of Civil Engineering, The University of Sydney, NSW 2006, Australia

ARTICLE INFO

Article history:
Received 10 January 2019
Received in revised form 15 March 2019
Accepted 2 April 2019
Available online 06 April 2019

Keywords:
Granular electrode structures
Effective conductivity
Resistor network method

ABSTRACT

To model the effective conductivity of the solid and the pore phase of a lithium-ion battery (LIB) we make use of the resistor network method (RN). We recall the scheme on how resistor networks can generally be set up and numerically solved. Furthermore, we explain how this general method can be applied to an assembly of spherical particles where for the individual resistances between touching particles an analytical formula is being used. As a new feature, we use the same scheme to setup resistor networks for the pore phase of an assembly of spherical particles where we propose a simple geometric approach for the calculation of the individual resistances of pore throats. For the validation of this method we created several random particle structures with different size distributions and calculated effective conductivities with both the RN and the finite element method (FEM). On the one hand, the comparison between RN and FEM shows a very good performance of the RN because the mean error lies within 4%. On the other hand, the RN results always lie within the well-known theoretical bounds for the effective conductivity in porous media. As an important aspect, the RN has proven to be highly efficient concerning the computation time and the resource costs.

1. Introduction

The microstructural composition of granular media strongly influences the effective transport properties, including thermal and electronic conductivity as well as diffusivity. For instance, the performance of granular-like structures, such as lithium-ion battery (LIB) electrodes, among other factors, is governed by the effective conductivity. On the one hand, the used material and its microstructure plays an important role, see for example [1,2]. On the other hand, the mechanical densification processes, such as calendering of the electrode or sintering of the particles, impact on the quality of the battery [3]. Throughout this work, we use LIB electrode structures as an example of a certain class of granular media where the effective conductivity plays an important role. The methods developed here can also be applied to other granular-like structures.

We consider the cathode of a LIB to be a porous microstructure composed of a solid and a pore phase. Usually, by densifying the microstructure the conductivity of the solid phase and hence the electronic conductivity can be enhanced. However, this also reduces the pore space and thus the ionic conductivity, see [4]. Since there has to be the adequate amount of electrons and lithium ions present for the reduction and oxidation reactions of lithium, the optimum balance between solid and pore phase conductivity has to be found.

During the past years, there have been a couple of theoretically and empirically driven theories to calculate the effective conductivity in porous media like the effective medium theory (EMT) [5–7] or by using empirical relations, e.g. [8]. Also, theoretical upper and lower bounds for the actual effective conductivity have been derived, as in [9]. Usually, the formulae take the form of functions of the porosity (or the packing factor) and the conductivity of the contributing phases.

Most of the time, when porous structures are being investigated the tortuosity parameter τ is taken into account. This parameter describes the deviation of the conducting paths from being straight lines. In the literature, the tortuosity parameter is sometimes treated differently, as the review in [8] shows. Since τ can not be measured directly, a couple of methods have been established. For example, in [10–12] the authors used the FIB/SEM tomography to look inside the microstructure of LIBs. The data was then reconstructed to be applicable to finite element method (FEM) or extended finite element method (XFEM) simulations to calculate the effective conductivity and hence the tortuosity of the solid phase.

The approach in [13] used networks of particles and resistances to calculate the effective thermal conductivity. For the calculation of the individual resistances between two contacting spheres they derived a fit-formula. Finally, they set up a system of linear equations for a steady-state heat problem by requiring all heat flux entering or leaving

* Corresponding author.
E-mail addresses: oleg.birkholz@kit.edu (O. Birkholz), yixiang.gan@sydney.edu.au (Y. Gan), marc.kamlah@kit.edu (M. Kamlah).

https://doi.org/10.1016/j.powtec.2019.04.005
0032-5910/

a particle to be zero. Solving this system of linear equations lead to the temperature gradient along the particle assembly and thus the effective conductivity could be calculated.

Similar to [13] the authors in [14] used resistor networks for the calculation of effective conductivity in solid oxide fuel cells (SOFC). Moreover, in [15,16] the resistor network method is being used for the calculation for the solid phase of both the SOFCs and LIBs. In the framework of the discrete element method (DEM), the effective thermal conductivity of granular packings has been investigated in [17–20].

A statistical approach has been chosen in [21] where the effective conductivity has been calculated by fit-function of volume fraction, tortuosity and constrictivity. The latter is a quantity which resembles the influence of bottlenecks inside the system. To this end, numerous microstructures have been generated and the effective conductivity, calculated by simulations using FEM, has been related to the fit-formula. The authors in [22] used a spatial partitioning technique which is called the Delaunay tessellation to discretize the pore phase. They converted the tessellated structure into a network with weighted edges to finally correlate its features, like the shortest paths, with permeability results obtained by FEM simulations. In an 3D stochastic approach, the effective thermal conductivity of porous metal fiber sintered sheets (PMFSS) have been modeled in [23]. Here, random fiber systems were generated and the effective thermal conductivity has been investigated using computational fluid dynamics (CFD) simulations.

In [24,25], random networks of throat resistances on regular grids were used to calculate effective conductivity. The individual resistances have been set either low or high [24] or they have been set following a certain distribution [25].

A system of linear equations has also been set up for the pore network of the gas diffusion layer in a polymer electrolyte membrane fuel cell in [26]. Here, a pore network has been modeled as a regular cubic grid where the nodes are the pores and the interconnecting edges are the throats. The throat sizes have been modeled following a truncated Weibull cumulative distribution.

Concerning the modeling of the electrical conductivity for the pore phase in porous media, the authors in [27] give a overview of the currently available methods.

In this work, however, we present the resistor network method (RN) for the calculation of effective conductivity for both the solid and the pore phase of a cathode structure inside lithium-ion batteries. In the first part of this work, in Section 2.1, we recall the resistor network method for the calculation of the effective conductivity. Further on, we show how we create such networks for the respective solid and pore phase of a granular system. Finally, we provide a general solving scheme for such resistor networks. In Section 2.2, the calculation of the single resistances is presented. Here, we employ and verify an analytical formula for the calculation of the resistance of two overlapping spheres. Also, we propose a spatial discretization method for the estimation of the representative resistance of a pore throat. Later, Section 3.1 contains the validation of the resistor network method, as described in the former sections. To this end, we used finite element methods on several randomly generated assemblies of spheres and compared the results to the values provided by the resistor network method. The resulting effective conductivities of both the FEM and RN method are then compared in Section 3.2. In Section 4.1 we check the validity of the calculated effective conductivities to the theories present in the literature. Further, in Section 4.2 we discuss the resource and time consumption for all conducted simulations for both methods.

Finally, in Section 5 we briefly summarize and conclude this work.

2. Methods

2.1. Resistor network method

In this section we explain the general idea behind the resistor network method (RN). The method, as used here, follows [28], where the so-called node potential method is introduced. It is being used to calculate electric circuits. We will illustrate the method first and will further describe how we use the RN to calculate the corresponding effective conductivity for both the solid and the pore phase of granular systems.

2.1.1. Conservation law and transport modeling

Generally, one considers conservation under steady-state conditions such that

$$\nabla \cdot \vec{F} = 0, \tag{1}$$

where $\vec{F}$ is the related flux vector. For the case of conservation of energy, this becomes

$$\nabla \cdot \vec{Q} = 0, \tag{2}$$

where $\vec{Q}$ is the heat flux vector, while for species conservation we have

$$\nabla \cdot \vec{J} = 0, \tag{3}$$

in which $\vec{J}$ is the species flux vector of diffusion. Furthermore, in the case of conservation of charge, we get

$$\nabla \cdot \vec{I} = 0, \tag{4}$$

with $\vec{I}$ being the current vector.

In the case of thermal transport, the heat flux vector is usually related to the negative gradient $-\nabla T$ of temperature T as the driving force by Fourier's law

$$\vec{Q} = -\boldsymbol{K}_{\mathrm{th}} \cdot \nabla T \tag{5}$$

as the constitutive law. Here, the thermal conductivity tensor $\boldsymbol{K}_{\mathrm{th}}$ characterizes the material under consideration. For diffusion, one often assumes Fick's first law

$$\vec{J} = -\boldsymbol{D} \cdot \nabla c \tag{6}$$

as constitutive law for the species flux in which $\boldsymbol{D}$ is the tensor of diffusion coefficients and c is the species concentration. On the other hand for, say, electronic transport, typically Ohm's law

$$\vec{I} = -\boldsymbol{G}_{\mathrm{el}} \cdot \nabla \varphi, \tag{7}$$

is taken to be the constitutive assumption by which the current depends on the negative gradient $-\nabla \varphi$ of electric potential φ as the driving force. Now, the electric conductivity tensor $\boldsymbol{G}_{\mathrm{el}}$ represents the material specific properties.

Irrespective of the underlying physical mechanisms, it becomes clear that the mathematical problems of thermal and charge transport posses the exact same structure. In the following, we exploit this analogy by transferring relations for thermal resistor to charge resistor network modeling. When focusing for the calculation of effective transport properties in porous materials on charge transport, may it be electronic or ionic, it is understood in view of the above discussion that the method presented here will also apply to diffusion which plays an important role in the context of lithium ion batteries, as well.

2.1.2. Mathematical formulation of a resistor network

In the following, the general idea behind the resistor network method is outlined. To this end, we consider the example network of nodes and resistors sketched in Fig. 1.

The nodes N^I, N^J and the currents $I^{I,J}$ between those nodes, respectively, are indicated in Fig. 1a. An yet unknown effective current I_{eff} is

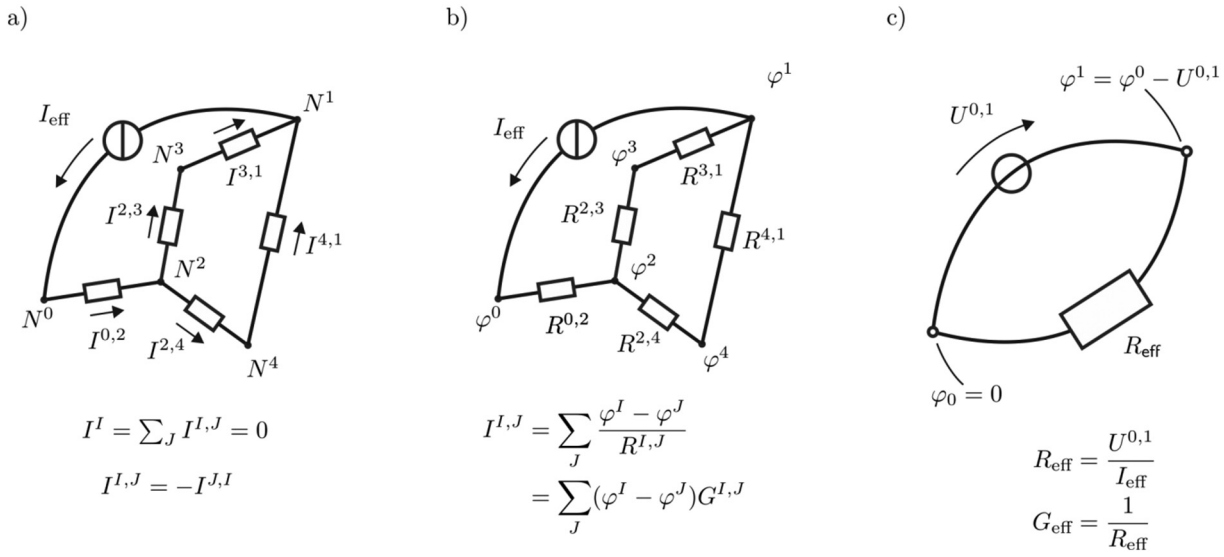

Fig. 1. General approach for the calculation of the effective conductivity on an exemplary electrical circuit using RN. a) Equivalent electrical circuit with nodes and edges with external and internal currents. b) Equivalent electrical circuit with resistors and external circuit. c) The values provided by the RN represent the effective resistance or conductance.

applied between the nodes N^0 and N^1 which results from a potential drop between those nodes. Note that we have chosen N^0 and N^1 such that all the other nodes lie between them. In other words, N^0 and N^1 represent the boundary nodes, i.e. the current collector nodes. At each node N^I, we combine Kirchhoff's current law

$$I^I = \sum_J^{n_{\text{neigh}}} I^{I,J} = 0, \tag{8}$$

accounting for the conservation of charge, and Ohm's law

$$I^{I,J} = \frac{U^{I,J}}{R^{I,J}} = \frac{\varphi^I - \varphi^J}{R^{I,J}}, \tag{9}$$

representing the constitutive property of the resistors. Here, n_{neigh} is the number of neighbors of node N^I and $U^{I,J}$ is the voltage between the nodes, represented by a potential drop $\varphi^I - \varphi^J$. As a result, we can write

$$I^I = \sum_J^{n_{\text{neigh}}} I^{I,J} = \sum_J^{n_{\text{neigh}}} \frac{\varphi^I - \varphi^J}{R^{I,J}} = \sum_J^{n_{\text{neigh}}} (\varphi^I - \varphi^J)\, G^{I,J} = 0 \tag{10}$$

to formulate equations for each node. Note that the directions of the currents in Fig. 1a can be chosen arbitrarily as long as the sign of each current in Eq. (10) is treated consistently. One choice would be that current $I^{I,J}$ pointing away from a node N^I has a negative sign.

According to Fig. 1b, the unknown potentials φ^I, φ^J correspond to the respective nodes N^I, N^J and $R^{I,J}$ is the resistance between the nodes. Also, we use the conductance $G^{I,J} = 1R^{I,J}$ as the reciprocal of the respective resistance. Now, we are able to assemble a linear system of equations for the given node resistor network.

In order to make the linear system of equations solvable, however, we replace the unknown current I_{eff} by an arbitrarily chosen potential drop $U^{0,1} = \varphi^0 - \varphi^1$ between the boundaries, see Fig. 1c. After solving the linear system of equations for the unknown potentials φ^I, the unknown effective current I_{eff} and therefore the effective resistance $R_{\text{eff}} = U^{0,1}/I_{\text{eff}}$ of the system can be calculated.

2.1.3. Application to the solid phase

In the approach followed here, every structure is approximated by discrete elements of different shapes possessing overall properties only, such as a uniform temperature, potential, or, as in he case of the DEM, velocity, and so on, see [29]. In this context, the most simple and therefore prominent shape is the sphere with only two parameters to fully characterize its geometry, namely the radius and the position.

To construct the node resistor network for a solid phase, discretized by spheres, conducting pathways have to be identified, in the first place. The so called percolated paths, which are highlighted in Fig. 2a can be found by first, identifying clusters of particles, see [30–32] and second, those clusters have to be selected which are connecting the boundaries on opposite sides.

As shown in the next Fig. 2b, the percolated clusters have to be converted to equivalent networks by assigning nodes and potentials φ^I, φ^J to the centroids of the particles and resistors $R^{I,J}_{\text{solid}}$ to the edges between those nodes. The latter can be achieved by certain geometric relations which will be introduced in Section 2.2.1. Finally in Fig. 1c, additional nodes have to be added to model the boundary nodes where the boundary conditions are imposed on. The result of this process leads to a node resistor network which is the basis for the calculation of the effective conductivity according to the scheme presented in Section 2.1.5.

2.1.4. Application to the pore phase

While it is quite straight forward to discretize the solid phase with discrete elements, it is not as obvious to discretize the pore phase in a similar way, because of the relatively complex shapes of the pores and throats. Here, we propose a way alternative to employing discrete particles to assign to the pore space and its throats nodes and edges with a corresponding resistance.

First, we need to identify pores and throats connecting two pores with each other. In previous publications, for example, a modified Delaunay tessellation approach is used for that purpose, see [22]. Here, it is said that it remains ambiguous what counts as a pore or a throat. As a workaround, the authors introduced an additional criterion upon which the decision is made. In the following we propose a method which overcomes this drawback.

To discretize the pore phase, we make use of the Voronoi tessellation method. In general, for isolated points in a domain, which happen in our case to be the nodes N^I, the Voronoi tessellation method assigns a spatial cell to each such point. Each cell contains all points whose distance to the associated cell node N^I is less than or equal to any other node N^J, $I \neq J$. In 3D space, the so-called Voronoi cells take the form of convex polyhedra. Using this method, the whole domain volume can be fully discretized. All points, i.e. particles, can be wrapped in cells and the borders, i.e. edges, of the cells lie in an optimum distance between particles.

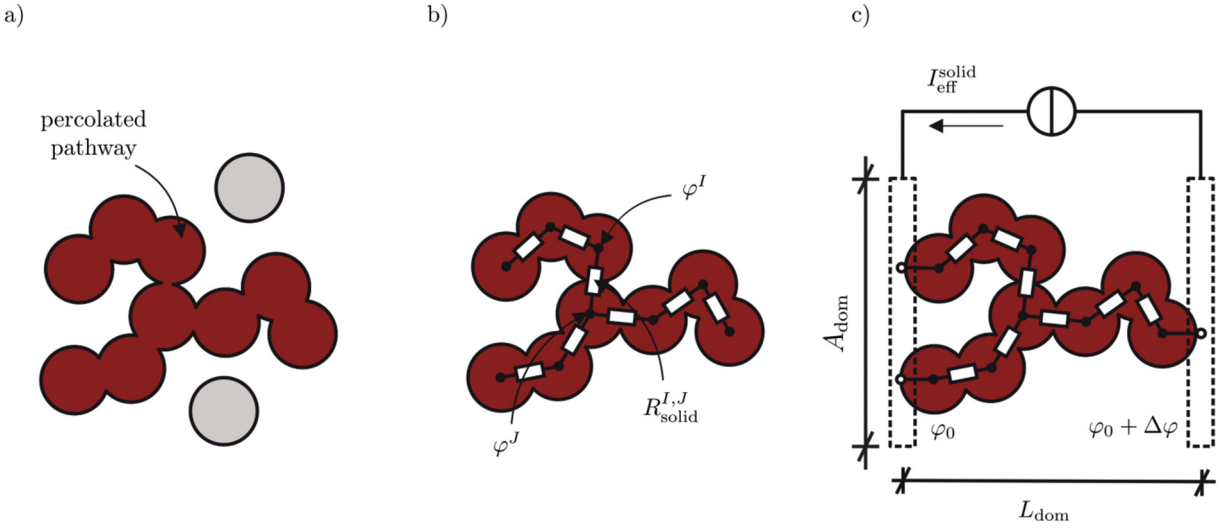

Fig. 2. Resistor network for the calculation of the effective conductivity of the solid phase. a) Percolating, i.e. conducting, pathways. b) Equivalent electrical circuit. c) Resistor network method (RN).

We employ the open source Voronoi tessellation library Voro++ [33], which additionally accounts for polydisperse particle sizes.

An exemplary Voronoi discretization can be seen in Fig. 3a. The spherical particles are wrapped by Voronoi cells, faces, edges and vertices. Conveniently, we choose each vertex as the centroid of a pore and the corresponding edges as the pore throats. Consequently, our network nodes correspond to the vertices where we assign the potentials φ^I, φ^J to and the edges will be related to resistances $R^{I,J}_{\text{pore}}$, see Fig. 3b.

Again, the boundary nodes have to be identified where the boundary conditions can be applied to, see Fig. 3c. Finally, the resulting node resistor network can be solved by the scheme described in Section 2.1.5.

2.1.5. Solution scheme

In the following, a general scheme for solving resistor networks according to Section 2.1.2 is presented. Due to the independence of the direction of the individual currents and therefore due to its generality, this method described bellow is well suited to be used in a computer program, see [28].

1) Create the conductivity matrix $\mathbf{G} = G_{ij}$ as

$$G_{ij} = \begin{cases} \sum_J^{n_{\text{neigh}}} G^{I,J} & \text{if} \quad i = j, \\ -G^{I,J} & \text{otherwise} \end{cases} \tag{11}$$

and the current vector $\vec{I} = I_j$ as

$$I_j = \begin{cases} I_{\text{eff}} & \text{if} \quad j = 0, \\ -I_{\text{eff}} & \text{if} \quad j = 1, \\ 0 & \text{otherwise}, \end{cases} \tag{12}$$

where $i, j = 0, 1, \ldots, n$, with n being the number of nodes. Furthermore, n_{neigh} is the number of neighbors of the individual node. As shown in

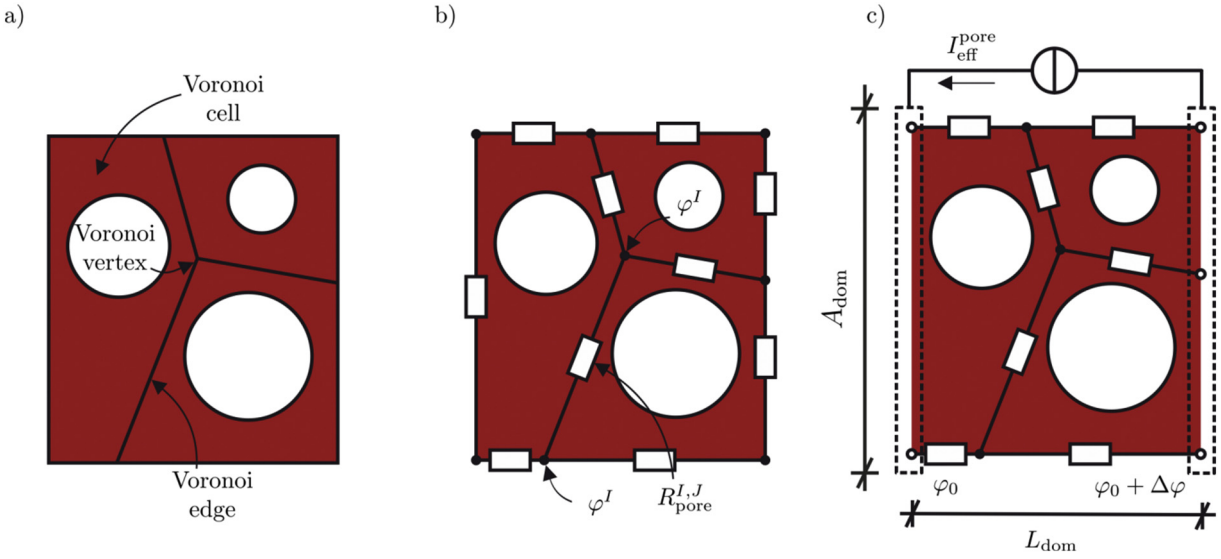

Fig. 3. Resistor network for the calculation of the effective conductivity of the pore phase. a) Voronoi tessellation of the percolating pore phase. b) Discretization of the pore phase using a Voronoi tessellation. c) Resistor network method (RN).

Fig. 1, I_{eff} is the current entering the network in node 0 and leaving the network at node 1. The resulting system of linear equations can be set up as

$$\underbrace{\begin{bmatrix} G_{00} & G_{10} & G_{20} & \cdots & G_{n0} \\ G_{01} & G_{11} & G_{21} & \cdots & G_{n1} \\ G_{02} & G_{12} & G_{22} & \cdots & G_{n2} \\ \vdots & \vdots & \vdots & \ddots & \vdots \\ G_{0n} & G_{1n} & G_{2n} & \cdots & G_{nn} \end{bmatrix}}_{\mathbf{G}} \underbrace{\begin{bmatrix} \varphi_0 \\ \varphi_1 \\ \varphi_2 \\ \vdots \\ \varphi_n \end{bmatrix}}_{\vec{\varphi}} = \underbrace{\begin{bmatrix} -I_{\text{eff}} \\ I_{\text{eff}} \\ 0 \\ \vdots \\ 0 \end{bmatrix}}_{\vec{I}}. \tag{13}$$

2) Next, we eliminate the unknown current I_{eff} from the right-hand side of Eq. (13). As a result, we create a modified system of linear equations which is smaller by one degree of freedom. To this end, we first make use of the equality $\varphi^0 = \varphi^1 + U^{0,1}$ and rewrite the first row in Eq. (13) as

$$\begin{bmatrix} G_{00} & G_{10} & G_{20} & \cdots & G_{n0} \\ G_{01} & G_{11} & G_{21} & \cdots & G_{n1} \\ G_{02} & G_{12} & G_{22} & \cdots & G_{n2} \\ \vdots & \vdots & \vdots & \ddots & \vdots \\ G_{0n} & G_{1n} & G_{2n} & \cdots & G_{nn} \end{bmatrix} \begin{bmatrix} \varphi_1 + U^{0,1} \\ \varphi_1 \\ \varphi_2 \\ \vdots \\ \varphi_n \end{bmatrix} = \begin{bmatrix} -I_{\text{eff}} \\ I_{\text{eff}} \\ 0 \\ \vdots \\ 0 \end{bmatrix}. \tag{14}$$

Secondly, we transfer the known voltage $U^{0,1}$ to the right-hand side which leads to

$$\begin{bmatrix} G_{00} & G_{10} & G_{20} & \cdots & G_{n0} \\ G_{01} & G_{11} & G_{21} & \cdots & G_{n1} \\ G_{02} & G_{12} & G_{22} & \cdots & G_{n2} \\ \vdots & \vdots & \vdots & \ddots & \vdots \\ G_{0n} & G_{1n} & G_{2n} & \cdots & G_{nn} \end{bmatrix} \begin{bmatrix} \varphi_1 \\ \varphi_1 \\ \varphi_2 \\ \vdots \\ \varphi_n \end{bmatrix} = \begin{bmatrix} -I_{\text{eff}} - G_{00}U^{0,1} \\ I_{\text{eff}} - G_{01}U^{0,1} \\ -G_{02}U^{0,1} \\ \vdots \\ -G_{0n}U^{0,1} \end{bmatrix}. \tag{15}$$

Third, we eliminate the unknown I_{eff} from the right-hand side of the second line by adding the first line. Further, we get rid of the redundant first line such that

$$\underbrace{\begin{bmatrix} G_{01} + G_{00} + G_{11} + G_{10} & G_{21} + G_{20} & \cdots & G_{n1} + G_{n0} \\ G_{02} + G_{12} & G_{22} & \cdots & G_{n2} \\ \vdots & \vdots & \ddots & \vdots \\ G_{0n} + G_{1n} & G_{2n} & \cdots & G_{nn} \end{bmatrix}}_{\hat{\mathbf{G}}} \underbrace{\begin{bmatrix} \varphi_1 \\ \varphi_2 \\ \vdots \\ \varphi_n \end{bmatrix}}_{\hat{\vec{\varphi}}} = \underbrace{\begin{bmatrix} -(G_{01} + G_{00})U^{0,1} \\ -G_{02}U^{0,1} \\ \vdots \\ -G_{0n}U^{0,1} \end{bmatrix}}_{\hat{\vec{I}}} \tag{16}$$

becomes the modified system of linear equations, where $\hat{\mathbf{G}}$ is the modified conductivity matrix, $\hat{\vec{\varphi}}$ is the modified potential vector and $\hat{\vec{I}}$ is the modified current vector.

3) Now,

$$\hat{\mathbf{G}}\hat{\vec{\varphi}} = \hat{\vec{I}} \tag{17}$$

can be solved for the modified unknown potential vector $\hat{\varphi}_j$.

4) In the next step, however, we need to adjust the potential values to the given boundary conditions, that is $\varphi_0 = 0$ and $\varphi_1 = \varphi_0 - U^{0,1}$, by adding the offset potential $\varphi_{\text{off}} = \varphi_1 - \hat{\varphi}_1$ to all $\varphi_{j>0}$

$$\varphi_j = \begin{cases} \varphi_0 & \text{if} \quad j = 0 \\ \hat{\varphi}_j + \varphi_{\text{off}} & \text{otherwise,} \end{cases} \tag{18}$$

for $j = 0, \ldots, n_{\text{nodes}}$ and reassign potential values φ_j to φ^J where the value of the index j corresponds to node number J.

5) In the last step, the unknown current I_{eff} can be calculated as the sum of all n_{neigh} currents entering current collector node N^0

$$I_{\text{eff}} = \sum_{J}^{n_{\text{neigh}}} \frac{\varphi^0 - \varphi^J}{R^{0,J}}. \tag{19}$$

When the effective current I_{eff} is known, the effective resistance R_{eff} and therefore the effective conductance G_{eff} or effective conductivity κ_{eff}, respectively, can be calculated by

$$R_{\text{eff}} = \frac{U^{0,1}}{I_{\text{eff}}} \quad \text{or} \quad G_{\text{eff}} = \frac{1}{R_{\text{eff}}}. \tag{20}$$

Finally, as we are interested in the effective conductivity, we have to take the domain dimensions into account. In the current work, we are considering a rectangular domain of a cross section A_{dom} and a length L_{dom} in any given direction such that the effective conductivity can be calculated as

$$\kappa_{\text{eff}} = G_{\text{eff}} \frac{L_{\text{dom}}}{A_{\text{dom}}} = \frac{I_{\text{eff}}}{U^{0,1}} \frac{L_{\text{dom}}}{A_{\text{dom}}} \quad \left[\frac{\text{S}}{m}\right]. \tag{21}$$

2.2. Calculation of the individual resistances

In Section 2.1 we introduced the resistor network method for the calculation of the effective conductivity for both the solid and the pore space, respectively. The crucial part of every resistor network, however, is the determination of the representative resistance values of the edges, where we only address geometrical throat effects.

For simplicity, we focus here on spherical particles. In addition to that and as mentioned before, we make use of the analogy between the mathematical form of thermal and charge transfer as well as diffusion problems, such that the methods we introduce for heat problems can directly be applied to charge transport and diffusion phenomena.

2.2.1. Resistance of two overlapping solid spheres

Section 2.1.3 describes resistor networks for the solid phase in a general way. For any given network, we now need to assign resistances to the edges, which happen to be contacting, i.e. overlapping spheres. There have been numerical and analytical investigations for the derivation of a formula where the resistance is a function of the geometric properties of the particles.

For two equal-sized spheres of the same material, the approximate resistance R_{fit} has been obtained by [16]. By analogy to [13] a fitting formula of the form

$$R_{\text{fit}} = \alpha \frac{r_p}{r_c} R_{\text{cyl}} \tag{22}$$

has been proposed. Here, R_{cyl} is the resistance of a cylinder with the radius r_p and the height d. The particles' radius is r_p and r_c depicts the contact radius between the two overlapping spheres. From a series of numerical finite element models, where the overlap was varied by increasing the radii of both spheres simultaneously at a fixed distance of their centers, the fitting constant α has been chosen as 0.952.

As a more general model, the analytical formula R_{anl} has been derived by [34] where the authors assume a steady state flow in a infinite or semi-infinite medium through a circular aperture and formulate the resistance as

$$R_{\mathrm{anl}} = \frac{1/\kappa^I + 1/\kappa^J}{4 r_c}. \tag{23}$$

Here, κ^I and κ^J are the bulk conductivities of the conducting materials and r_c is the radius where the flux flows through. The contact radius r_c is obtained from the circle in the throat of the two overlapping spheres in contact. If as a special case one sets the conductivity equal to $\kappa^I = \kappa^J = \kappa^p$, Eq. (23) reduces to the solution

$$R_{\mathrm{anl}} = \frac{1}{2 r_c \kappa^p} \tag{24}$$

given in [35].

Fig. 4a shows the comparison of the results of the two formulae to each other. As a reference, we take results from FEM simulations that we calculated by ABAQUS [36]. The finite element method gives us the spatially resolved solution of the stationary boundary value problem for two spheres in contact as shown in Fig. 4b. It consists of the partial differential equation obtained from the balance relation, Eq. (2), and the constitutive equation, Eq. (5), on the one side and of the boundary conditions on the other side. By sufficient mesh refinement, the finite element solution can be considered to be exact according to the needs.

In Fig. 4b, two half-spheres with the radii r^I and r^J and their bulk conductivities κ^I and κ^J, respectively, are shown. While, for simplicity, radius and conductivity are taken as unity for one sphere, they are chosen according to a prescribed ratio for the other. The half-spheres are overlapping to form the contact radius r_c. Next, a temperature gradient ΔT is imposed on the middle surfaces of the spheres such that a flux $\vec{q}$ emerges. For simplicity, the temperature drop is chosen as unity. In order to calculate the resulting resistance R_{num}, the resulting total flux Q_{num} at the middle surface of one of the spheres is used to finally obtain

$$R_{\mathrm{num}} = \frac{\Delta T}{Q_{\mathrm{num}}}. \tag{25}$$

A series of FEM simulations have been carried out, where not only the radius ratios r^I/r^J and the contact radius relative to the smaller sphere r^J/r_c had been varied but also the bulk conductivity ratios k^I/k^J. In Fig. 4a, the dimensionless representation of the resistance

$$\tilde{R} = \frac{R r^I}{1/\kappa^I + 1/\kappa^J} \tag{26}$$

is plotted versus the dimensionless contact radius r^J/r_c for three arbitrarily chosen cases but with relatively extreme ratios.

It can be seen that in the regime of a rather large relative contact radius of $r^J/r_c < 5$, both formulae perform quite similar to each other and to the FEM solution. However, if the relative contact radius increases towards $r^J/r_c = 20$, which means that the contact radius is merely 5% of the particles radius, only R_{anl}, according to Eq. (23), is in a good agreement with the FEM reference solution whereas R_{fit} increasingly overestimates the resistance. Furthermore, it has to be noted that Eq. (23) even fits well with the FEM reference results when the radius ratio r^I/r^J has been varied from 1/1 to 1/100 and the conductivity ratio κ^I/κ^J has been varied from 1/1 to 1/300 and 300/1. Here, the analytical formula underestimates the numerical solution by a mean error of around $\bar{e} = 4\%$.

In view of the above findings, we conclude that the formula according to Eq. (23) has been successfully verified as a general model of the resistance of two spheres in contact. Thus, in this work we have chosen Eq. (23), according to [34], for the calculation of a single contact resistance between two spheres because the variation of radius ratio as well as a variation of conductivity ratio is intrinsically accounted for.

2.2.2. Resistance of a pore throat element

As a point of departure for modeling the resistance of the pore phase in a granular assembly, we assume that transport is merely hindered by the bottlenecks created by the solid particles. To model such bottlenecks or pore throat elements, we need to identify the pores and pore centers first.

Fig. 5a exemplarily shows the first step, as we use the so-called Voronoi tessellation according to [33], as explained in Section 2.1.4. We recall that we partition the whole volume into cells containing each particle and consisting of faces, edges and vertices. The region of a cell outside its particle is its fraction of the pore phase. Conveniently, we choose the vertices to be the nodes N^I, N^J and therefore

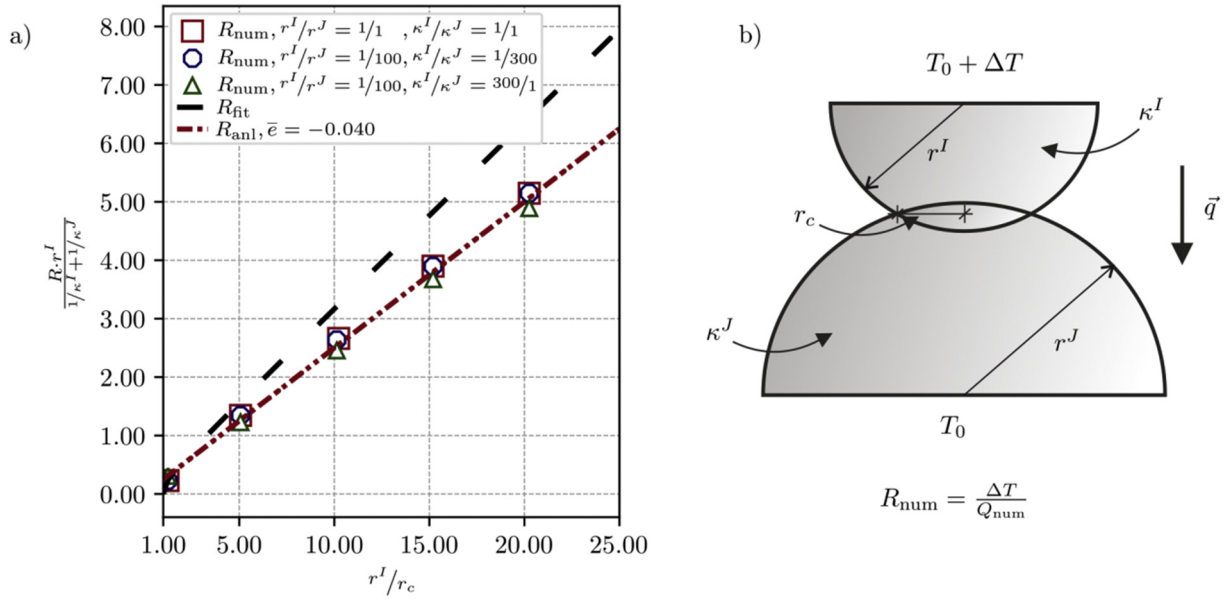

Fig. 4. a) Comparison of numerical FEM results to the analytical formulae (22) and (23). b) Sketch of the FEM model where a temperature gradient is imposed on two overlapping half-spheres of different sizes and conductivities to evaluate the resulting heat flux.

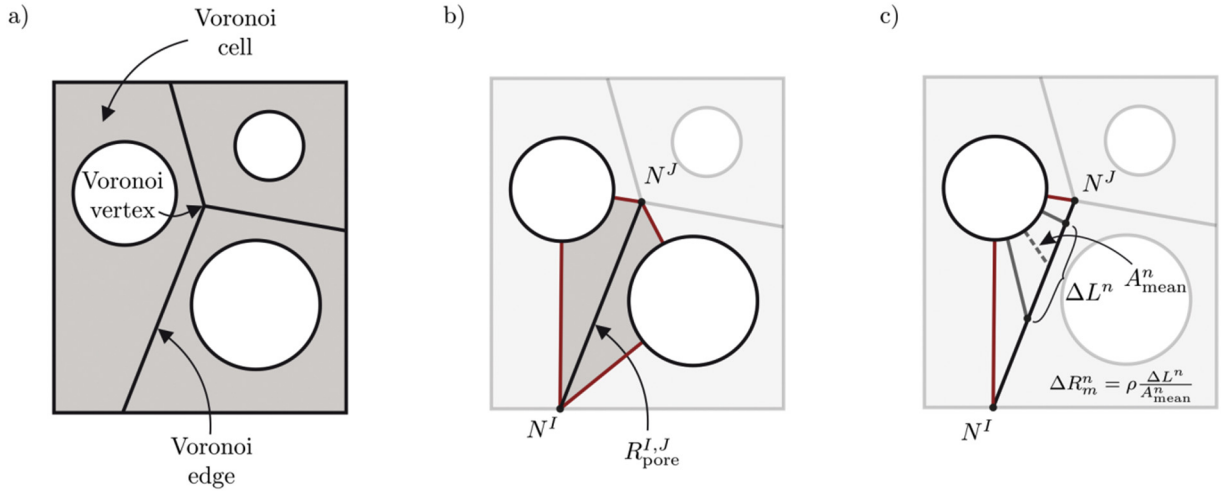

Fig. 5. Modeling pores and pore throat elements. a) Discretization of the pore phase into Voronoi cells. b) Voronoi edges and the correspoinding surrounding volume, i.e. throat elements, connecting Voronoi vertices, i.e. pores. c) Partitioning of throat elements into wire resistances of incremental lengths.

the centers of the pores where we assign the potentials φ^I, φ^J to. Consequently, we consider the connecting edges as the pore throat elements weighted by certain resistances $R^{I,J}_{\text{pore}}$. In Fig. 5b, the gray shaded area indicates the throat element enclosed by the nodes of the edges and the centers of the corresponding particles, from which we will calculate the representative resistance. Obviously, in the 2D example of Fig. 5, the resistance between nodes N^I and N^J is a parallel connection of two resistances, i.e. throat sub-elements, constituted by two neighboring cells. Now, the resistance resulting from one such sub-element is calculated as a sufficiently fine discretized series connection of wire resistances.

To be specific, we divide each edge into sufficiently small increments ΔL^n and calculate the resistance ΔR^n_m of each segment by

$$R = \rho \frac{L}{A} \quad \Rightarrow \quad \Delta R^n_m = \rho \frac{\Delta L^n}{A^n_{\text{mean}}}, \tag{27}$$

where ρ is the resistivity and $A^n_{\text{mean}} = 12(A^n + A^{n+1})$ is the mean cross section area for the n'th increment. For the geometric calculation of the respective cross sections we make use of the well-known Boost and CGAL library [37,38].

The resulting resistance $R^{I,J}_m$ of one sub-element is then calculated as a series connection of the incremental resistances as

$$R^{I,J}_m = \sum_{n=1}^{n_{\text{incr}}} \Delta R^n_m = \rho \sum_{n=1}^{n_{\text{incr}}} \frac{\Delta L^n}{A^n_{\text{mean}}}, \tag{28}$$

where n_{incr} is the number of increments used along I and J. Here, ΔL is estimated individually for each sub-element. The size of ΔL is incrementally reduced until the resulting resistance of the next increment doesn't differ from the previous one by a certain small threshold, here within 5%. Finally, as mentioned above, we calculate the resulting resistance $R^{I,J}_{\text{pore}}$ of the edge, i.e. the throat element, connecting nodes N^I, N^J, i.e. the pores, as a parallel connection of the resistances $R^{I,J}_m$ of all m_{selmn} sub-elements containing this edge by

$$R^{I,J}_{\text{pore}} = \left(\sum_{m=1}^{m_{\text{selmn}}} \frac{1}{R^{I,J}_m} \right)^{-1}. \tag{29}$$

Thus, we have derived a model for the throat element resistances in the resistor network method when modeling the pore phase. Validation of the method, solid phase and pore phase, is now the subject of the next section.

3. Results

3.1. FE-model for the validation of the resistor network method

In the following, the validation of the resistor network method, as used here, is explained. To this end, we compared the RN results for the effective conductivity of both the pore and the solid phase to finite element results using ABAQUS [36]. We generated random spherical assemblies and used the exact same geometry for both of the methods, see Fig. 6. As far as the finite element simulations are concerned, the geometry is spatially resolved and the boundary value problem of the partial differential equation of the stationary transport obtained from the balance relation, Eq. (2), and the constitutive equation, Eq. (5), is solved. Because of the absence of fully analytical formulae for random spherical particle assemblies, we thus consider, as before, the FEM results to be the exact solution of the transport properties. With that said, the finite element results serve as benchmark for findings by the resistor network method.

The generation of the assemblies was done in two steps. First, the initial structure was generated using an algorithm similar to the random close packing algorithm (RCP) [39]. In general, the RCP produces a randomly distributed, densely packed and overlap-free collection of spheres. Following the approach of [17,40], the algorithm has been extended to account for any given size-distribution of the particles, i.e. the radii of the spheres. The size-distribution of the spheres corresponds to a normal distribution with a given mean radius r_{mean} and standard deviation r_σ. Secondly, the initial structure was densified using an algorithm which we call numerical sintering [15,16]. During this process the radii of the spheres inside the assembly are iteratively increased while keeping the centroids fixed in space. It is important to note that during the densification routine we neglect any sorts of mechanics, i.e. contact forces and alike. After every iteration, a given threshold is checked which indicates that the wished densification state is reached. In our case, the threshold was defined in terms of the mean contact angle θ_{mean}. Here, θ_{mean} is defined as the mean of all contact angles of the considered assembly of spheres. A single contact angle of two overlapping spheres is taken as the bigger of the two angles enclosing the contact radius.

The geometrical data of the spheres were then imported into a box-shaped simulation domain where the parts of the spheres outside of the domain boundaries were cut off, as can be seen in Fig. 6b. In both, the FEM and the RN analysis, we consider transport through two opposite surfaces of our box-shaped simulation domain. Either the particle phase, i.e. the solid phase, or the pore phase has been analysed. Concerning the finite element simulations, for the phase of interest, all nodes on one of these surfaces were set to the same temperature,

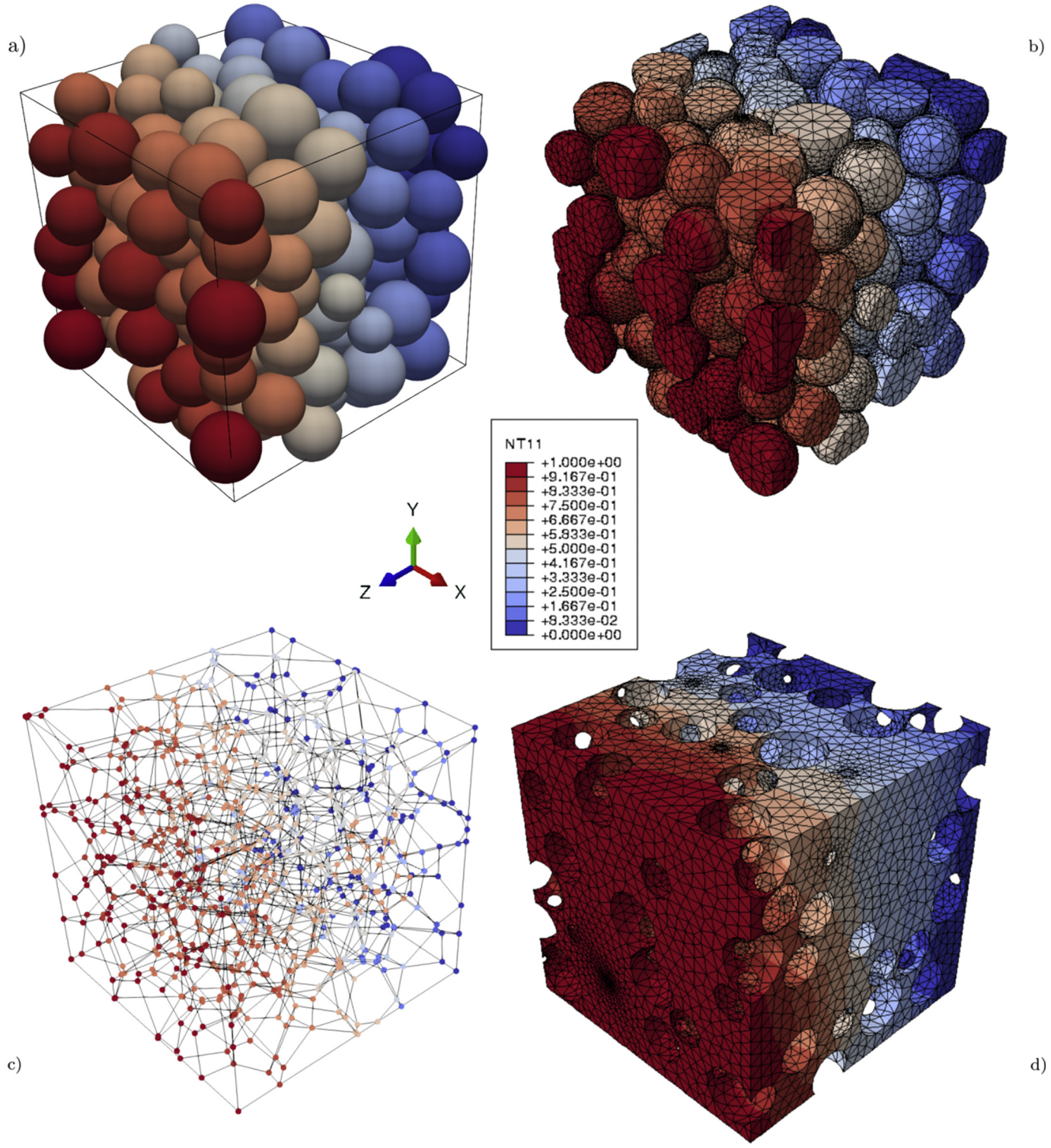

Fig. 6. Discrete element and finite element models of one of the polydisperse sphere packings. a) Temperature equivalent potential distribution along the z-direction of the solid phase solved using the resistor network method. b) Temperature distribution along the z-direction of the solid phase solved using the finite element method. c) Temperature equivalent potential distribution along the z-direction of the pore phase using the resistor network method. d) Temperature distribution along the z-direction of the pore phase using the finite element method.

while the temperature of the nodes on the opposite surface were dropped by $\Delta T = 1$ with respect to this temperature. The other four surfaces of the box-shaped simulation domain were assumed to be insulated, and thus, they are parallel to the direction of overall flux. The steady-state heat transfer problem was solved exactly by FEM using quadratic DC3D10 elements. The resulting heat flux Q_{FEM} through either the solid phase or the pore phase was obtained at one of the surfaces with the applied temperature. By knowing the domain length L_{dom} and cross section area A_{dom}, in the corresponding directions, we were able to calculate the effective conductivity of the phase of interest as

$$\kappa_{\mathrm{FEM}}^{\mathrm{eff}} = \frac{Q_{\mathrm{FEM}}}{\Delta T}\frac{L_{\mathrm{dom}}}{A_{\mathrm{dom}}}. \tag{30}$$

Table 1
Left: Structural parameters of the spherical packings for the validation models. Right: Resulting parameters after the densification process.

Type	$n_{\text{particles}}$	r_{mean}	r_σ	θ_{mean}	$\phi_{\text{solid, mean}}$	$\phi_{\text{pore, mean}}$	$r_{\text{c, mean}}$
1	200	1.00	0.00	20	0.68	0.32	0.34
2	200	1.00	0.10	20	0.66	0.34	0.32
3	200	1.00	0.25	20	0.65	0.35	0.30

Concerning the resistor network method, on the other hand, the generated assemblies of spheres can be imported without further adjustments. Depending on the transport phase considered, the node resistor networks were created following either the method in Section 2.1.3 for the solid phase or the method in Section 2.1.4 for the pore phase. Further, for the resulting networks a potential drop of $\Delta\varphi = 1$ was imposed on the nodes of two opposing surfaces while for the nodes of the other surfaces no boundary conditions were applied. Again, by considering the domain length and cross section area the effective conductivity can be calculated via

$$\kappa_{\text{RN}}^{\text{eff}} = \frac{I_{\text{eff}}}{\Delta\varphi}\frac{L_{\text{dom}}}{A_{\text{dom}}}, \tag{31}$$

where the effective current I_{eff} was calculated using the resistor network solving scheme according to Section 2.1.5.

In our approach, we calculate the influence of geometry of a granular system using a unit value of the bulk transport property for the material. All results shown, either FEM or RN, in this paper refer to such a unit bulk property. Subsequently, these normalized values have to be multiplied by the corresponding bulk transport property of the material under consideration in order to obtain the effective transport property of the related granular system.

Fig. 6 shows an example of a randomly generated sphere packing with a polydisperse size-distribution according to assembly type 3 in Table 1. In Fig. 6a the discrete element model of the solid phase is presented. Additionally, the temperature equivalent potential distribution in the z-direction provided by the resistor network method is indicated by the color. In Fig. 6b the finite element model of the solid phase is shown. Here, the color refers to the spatially resolved temperature distribution in z-direction. The nodes and edges assigned to the pore phase by our new RN method can be seen in Fig. 6c, and the temperature equivalent potential distribution is indicated by the color of the nodes. In Fig. 6d the FEM discretization of the pore phase is shown and once more the temperature distribution in z-direction is indicated by the color.

In Table 1, the parameters for the conducted studies can be seen. Up to five cases per assembly type have been generated. Here, the number of particles is given by $n_{\text{particles}}$, while the mean radius and the standard deviation is described by r_{mean} and r_σ, respectively. The state of densification is depicted by the mean contact radius of the solid phase θ_{mean}. On the other hand, the resulting packing factor ϕ_{solid} and the porosity $\phi_{\text{pore}} = 1 - \phi_{\text{solid}}$ as well as the mean contact radius $r_{\text{c, mean}}$ can be seen.

3.2. Evaluation of the results

Fig. 7 shows the comparison between resistor network and finite element results for each study with the results for the solid phase in Fig. 7a, and the results for the pore phase in Fig. 7b. The effective conductivity is normalized by the corresponding bulk conductivity. For each case, the normalized effective conductivity of the RN results $\hat{\kappa}_{\text{RN}}$ is plotted over the normalized effective conductivity of the FEM solution $\hat{\kappa}_{\text{FEM}}$. Thus, the bisecting solid 1:1 line indicates a perfect match between both methods whereas a deviation above or below means an over- or underestimation of the RN results compared to the FEM results, respectively. Examining Fig. 7a and b, a couple of observations can be made.

First of all, concerning the results for the solid phase, the RN values deviate from the FEM results by a mean error lower than $\bar{e} = 4\%$. This comes as no surprise, since every contact between two spheres, i.e. resistance, inside the assembly is calculated by an analytically derived formula, see details in Section 2.2.1, which is the exact solution. On the other hand, the deviation of the results by the resistor network for the pore phase also deviate by a relatively low mean error of around $\bar{e} = 3$ %. We consider this degree of agreement with our reference solution as a successful verification of our simplifying RN approach for the pore phase.

Another observation is the evolution of the effective conductivity between the different assembly types. With decreasing packing factor from $\phi_{\text{solid, mean}}^{\text{type1}} = 0.68$ to $\phi_{\text{solid, mean}}^{\text{type3}} = 0.65$ going from assembly type 1 to 3, the effective conductivity for the solid phase is decreasing. The opposite behavior can be seen for the effective conductivity of the pore phase. On the other hand, the resistor network method allows a more detailed explanation, as will be discussed now.

For the solid phase, we showed in Section 2.2.1 that we calculate the resistances of individual overlapping spheres using Eq. (23), which is a function of the contact radius r_c. Now, for constant mean contact angle θ_{mean} and increased standard deviation for the radii, one can see in

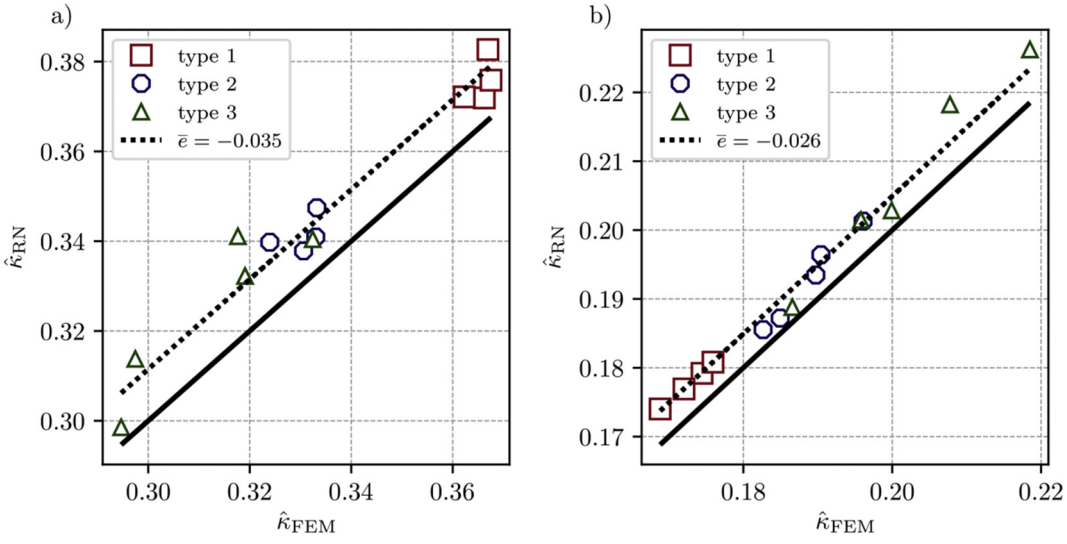

Fig. 7. Comparison of FEM results with RN results for polydisperse particle assemblies. Effective conductivity of the (a) solid phase and (b) the pore phase.

Table 1 that the mean contact radius is decreasing from $r_{c,\,\mathrm{mean}}^{\mathrm{type1}} = 0.34$ to $r_{c,\,\mathrm{mean}}^{\mathrm{type3}} = 0.30$. This leads to higher individual resistances, as contact radii appear in the denominator in the formula (23), and thus to lower effective conductivities for the solid phase along with it.

For the pore phase, it is difficult to derive a similar explanation since the formula for the resistance of a pore throat, as in Eq. (29), is more complex, see Section 2.2.2. However, it is obvious to see that the individual resistance is inversely proportional to the incremental cross section areas, i.e. the porosity of the assembly. In other words, an increasing porosity leads to an increase in the average cross section area of the pore throats and thus to a higher effective conductivity for the pore phase.

4. Discussion

In the following, we check the validity of the effective conductivities provided by the resistor network method, as presented here, against well-known theories found in literature. To this end, some of the theories are briefly recalled first and then compared to the results which were provided in Section 3.2. Further explanation on the theories can be found in [5]. Finally, we take a glance on the computational costs of the simulations conducted in 3.2 of the RN and compare it to the FEM.

4.1. Comparison to theories in literature

First, a narrow bounds for the effective conductivity were presented by Hashin and Shtrikman [9]. These well-known bounds were derived by variational theorems for the effective magnetic permeability but due to the mathematical analogy the results can also be applied to electric or thermal conductivity in which case they read as

$$\begin{aligned}\kappa_{\mathrm{eff}}^{\mathrm{hs1}} &= \kappa_{\mathrm{solid}}\frac{2\kappa_{\mathrm{solid}}+\kappa_{\mathrm{pore}}-2\left(\kappa_{\mathrm{solid}}-\kappa_{\mathrm{pore}}\right)\phi_{\mathrm{pore}}}{2\kappa_{\mathrm{solid}}+\kappa_{\mathrm{pore}}+\left(\kappa_{\mathrm{solid}}-\kappa_{\mathrm{pore}}\right)\phi_{\mathrm{pore}}}\\ \kappa_{\mathrm{eff}}^{\mathrm{hs2}} &= \kappa_{\mathrm{pore}}\frac{2\kappa_{\mathrm{pore}}+\kappa_{\mathrm{solid}}-2\left(\kappa_{\mathrm{pore}}-\kappa_{\mathrm{solid}}\right)\left(1-\phi_{\mathrm{pore}}\right)}{2\kappa_{\mathrm{pore}}+\kappa_{\mathrm{solid}}+\left(\kappa_{\mathrm{pore}}-\kappa_{\mathrm{solid}}\right)\left(1-\phi_{\mathrm{pore}}\right)}.\end{aligned} \tag{32}$$

It should be noted, that for $\kappa_{\mathrm{solid}} > \kappa_{\mathrm{pore}}$ the equation with the super-script hs1 becomes the upper bound and thus the equation with the super-script hs2 becomes the lower bound. In case of $\kappa_{\mathrm{solid}} < \kappa_{\mathrm{pore}}$ the upper and lower bounds are interchanged.

Next, in the framework of the effective medium theory (EMT) Landauer presented in [41] by assuming a system of two randomly distributed phases the formula

$$\begin{aligned}\kappa_{\mathrm{eff}}^{\mathrm{emt}} = 1/4\Big(&\left(3\phi_{\mathrm{pore}}-1\right)\kappa_{\mathrm{pore}}\\ &+\left[3\left(1-\phi_{\mathrm{pore}}\right)-1\right]\kappa_{\mathrm{solid}}+\sqrt{\left(3\phi_{\mathrm{pore}}-1\right)\kappa_{\mathrm{pore}}}\\ &\overline{+\left(3\left\{1-\phi_{\mathrm{pore}}\right\}-1\right)\kappa_{\mathrm{solid}}^2+8\kappa_{\mathrm{solid}}\kappa_{\mathrm{pore}}}\Big)\end{aligned} \tag{33}$$

for the calculation of the effective conductivity.

In Fig. 8a, we see the comparison of the effective conductivity for the solid phase provided by the resistor network method to the theories according to Eqs. (32) and (33). Since the pore phase in this case doesn't contribute to the transport we set $\kappa_{\mathrm{pore}} = 0$. Thus the lower bound $\kappa_{\mathrm{eff}}^{\mathrm{hs2}}$ is zero for all $\phi_{\mathrm{pore}} > 0$.

Furthermore, in Fig. 8b we see the comparison of the effective conductivity for the pore phase provided by the resistor network method to the above mentioned theories. This time, the solid phase doesn't contribute to the transport and therefore we set $\kappa_{\mathrm{solid}} = 0$ which results in the lower bound $\kappa_{\mathrm{eff}}^{\mathrm{hs1}}$ to be zero for $\phi_{\mathrm{pore}} > 0$.

It can be seen that for both cases, i.e. conducting solid or pore phase, the results provided by the resistor network method always lie between the Hashin-Shtrikman bounds and therefore, form the viewpoint of these theories, in a reasonable range. Further, it should be mentioned that for the given cases the EMT yields different results compared to the RN. As it is shown in Fig. 8a, the EMT overestimates the RN values. On the other hand, the effective medium theory underestimates the effective conductivity of the pore phase calculated by the resistor network method, as can be seen in Fig. 8b. Also, in accordance with both of the theories, with increasing porosity the effective conductivity is either decreasing, see Fig. 8a, or increasing, see Fig. 8b.

Finally and most important, we recall that for the considered particle assemblies the RN results perform very well for both the pore and the solid phase as compared to exact FEM simulations. Also, the RN is capable to predict the effective conductivity even for rather complex particle assemblies, i.e. polydisperse and overlapping spheres, where theories like the effective medium theory would not be fully applicable anymore. In any case, the results from the resistor network approach, as used here, reside within the well-known Hashin-Shtrikman bounds.

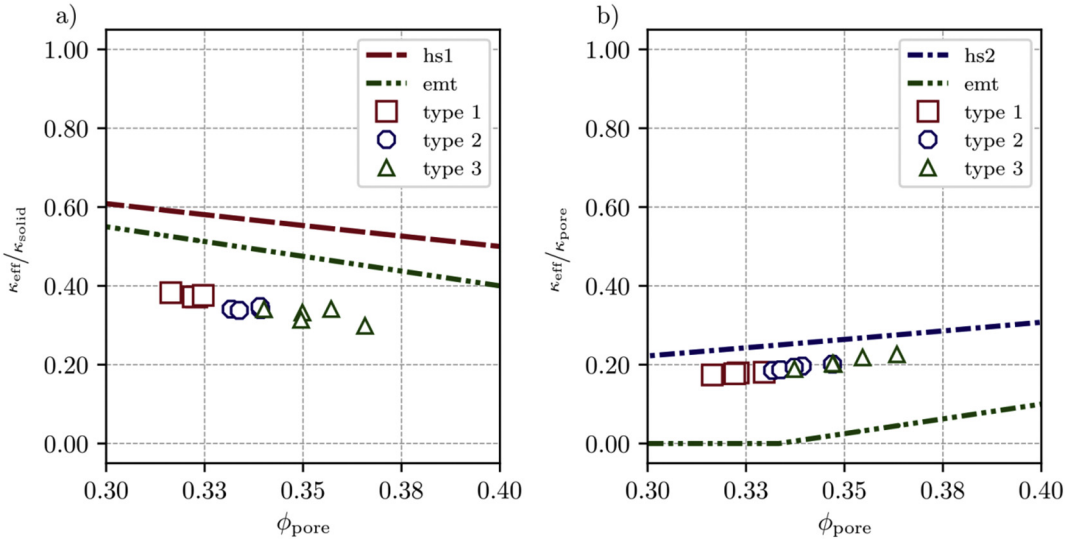

Fig. 8. Comparison of the RN results with theoretical bounds of the effective conductivity for porous media. a) Effective conductivity of the solid phase b) Effective conductivity of the pore phase.

Table 2
Comparison of resource costs RN versus FEM for the solid phase calculations.

Method	Mean number of nodes	CPUS / Threads used	Total RAM (MB)	Simulation time (mins)
RN	≈250	1 thread	≈100	≈1
FEM	≈650,000	4 CPUs	≈8000	≈73

Table 3
Comparison of resource costs RN versus FEM for the pore phase calculations.

Method	Mean number of nodes	CPUS / Threads used	Total RAM (MB)	Simulation time (mins)
RN	≈1100	4 threads	≈2000	≈3
FEM	≈300,000	4 CPUs	≈6000	≈32

4.2. Computational performance

From the computational perspective, the resistor network method promises to be more efficient in terms of resource and time cost compared to the finite element method. That is because for the RN method the number of degrees of freedom (DoF) corresponds directly to the number of particles whereas for the FEM the spatially resolved mesh increases the number of DoF.

In the following, we want to compare the actual facts concerning the computation time and resource cost for the 3 studies with 5 cases, that is 15 simulations, we have calculated in Section 3.1. We used a workstation with Intel(R) Xeon(R) CPU E5-1620 v3 @ 3.50 GHz with 32 GB ram specifications. For the calculations of the resistor networks, we used an partially parallelized in-house code *kitGran* written in C++ and based on the work by [17], where we made use of a couple of open-source libraries. Here, the *CGAL* and *Boost* library [37,38] helped to perform all sorts of three-dimensional geometry operations, the Voronoi tessellation library *Voro++* [33] delivered the Voronoi cells for our RN method for the pore phase and the linear algebra library *Eigen* [42] was used to set up and solve the sparse system of linear equations.

Remarkably, the resistor network method performs extremely well for the solid phase. Here, with just 250 nodes and negligibly low resource costs, see Table 2, it outperforms the computational performance of the finite element method. Here, it takes the FEM 73 min and 4 CPUs whereas the RN method delivers the result with 1 thread within 1 min. Moreover, the finite element method needed around 650,000 nodes to discretize the model which is relatively large compared to 250 nodes used for the resistor network method. This comparably large amount of nodes can be explained by the fact that for slightly overlapping spheres the contact areas become relatively small. In this cases, the element sizes become small as well, thus resulting in an increase of node numbers. Due to the way the resistances, i.e. overlaps of spheres, are calculated for the resistor networks, see Section 2.2.1, we implicitly account for relatively small contact areas without the need for more detailed discretization.

As can be seen in Table 3, for the pore phase the RN also performed better compared to the FEM. Here, the FEM model needed around 300,000 nodes on average to discretize the pore phase. Furthermore, it took 4 CPUs over 32 min and 6000 MB in total to calculate the results. On the other hand, the RN method needed 1100 nodes on average to capture the same problems and delivered results within 3 min while using 2000 MB memory space.

5. Conclusion

In this work, we presented a resistor network method for the calculation of the effective transport properties for both the solid and pore phase in porous media, e.g. a cathode of a lithium-ion battery. First, we have shown how for both cases equivalent node and edge networks can be constructed and second, how representative resistors can be calculated for the edges. Further, the general setup and solution scheme for the resistor networks has been presented. The method has been validated by finite element methods for different random assemblies of spheres with increasing polydispersity.

With the resistor network method being applicable for the solid and pore phase and having significant computational efficiency, it has proven to be a valuable asset for the fast estimation of the effective conductivity of granular media. Therefore, it can be used for Monte Carlo simulations to study the influence of the microstructure on the effective properties of porous media, e.g. cathodes in lithium-ion batteries. At a much larger scale, the effective properties can be used for developing microstructure-informed cell models.

It should be mentioned that we focused on purely geometrical throat effects here. Additional interface resistances can be included in a similar framework, once the related physical information and material characterization are available from either experiments or detailed modeling.

On the one hand, the calculation of the effective conductivity of non-spherical particles in contact has already been investigated, see e.g. [20]. There, the particle to particle resistance has been described as a function of the semi-axes of the contact ellipse. On the other hand, the calculation of the transport properties of the pore phase of non-spherical particles - in the framework used here - needs more investigation. In particular, the used tessellation technique not only needs to account for the particle size but also for the shape to properly discretize the pore phase. In the view of the above findings, the resistor network method for the calculation of the effective transport properties of both the solid and the pore phase can be regarded as validated by spatially resolved finite element methods. Compared to the RN used in [13–16], the calculation of the resistance of two overlapping spheres was enhanced by using the more general formula, Eq. 23, which also was validated using FEM. Moreover, the proposed method for the calculation of the pore phase overcomes certain drawbacks of different network methods. As described in Section 2.2.2 for example, no additional assumptions have to be made to distinguish between pore and throat as is the case in [22]. Also, the distribution of the throat resistances results directly from the geometry of the solid phase. Thus, the influence of microstructure of the solid phase on the effective conductivity of the pore phase can be investigated.

In the context of lithium-ion batteries, the resistor network method developed here, when applied to the solid phase, can be used to calculate the electronic conductivity of a multiphase system consisting of, say, active material and conductive additives. On the other hand, when applied to the pore phase, it can be used to calculate the effective diffusion coefficient, as well as the effective ionic conductivity of the liquid electrolyte phase. In each case, the effective transport properties can be obtained by RN with respect to the geometry. The effective conductivity or diffusivity of the system, on the other hand, can then be directly calculated using the respective bulk properties of the materials under consideration.

References

[1] S.-T. Myung, M.H. Cho, H.T. Hong, T.H. Kang, C.-S. Kim, Electrochemical evaluation of mixed oxide electrode for Li-ion secondary batteries: Li1.1mn1.9o4 and LiNi0.8co0.15al0.05o2, J. Power Sources 146 (1) (2005) 222–225, https://doi.org/10.1016/j.jpowsour.2005.03.031, http://www.sciencedirect.com/science/article/pii/S0378775305003988.
[2] D.-C. Li, T. Muta, L.-Q. Zhang, M. Yoshio, H. Noguchi, Effect of synthesis method on the electrochemical performance of LiNi1/3mn1/3co1/3o2, J. Power Sources 132 (1) (2004) 150–155, https://doi.org/10.1016/j.jpowsour.2004.01.016, http://www.sciencedirect.com/science/article/pii/S0378775304000801.
[3] D. Schmidt, M. Kamlah, V. Knoblauch, Highly densified NCM-cathodes for high energy Li-ion batteries: microstructural evolution during densification and its influence on the performance of the electrodes, J. Energ. Stor. 17 (2018) 213–223, https://doi.org/10.1016/j.est.2018.03.002, http://www.sciencedirect.com/science/article/pii/S2352152X17305960.
[4] Y.H. Chen, C.W. Wang, X. Zhang, A.M. Sastry, Porous cathode optimization for lithium cells: ionic and electronic conductivity, capacity, and selection of materials, J. Power

Sources 195 (9) (2010) 2851–2862, https://doi.org/10.1016/j.jpowsour.2009.11.044, http://www.sciencedirect.com/science/article/pii/S0378775309020527.
[5] J.K. Carson, S.J. Lovatt, D.J. Tanner, A.C. Cleland, Thermal conductivity bounds for isotropic, porous materials, Int. J. Heat Mass Transf. 48 (11) (2005) 2150–2158, https://doi.org/10.1016/j.ijheatmasstransfer.2004.12.032, http://www.sciencedirect.com/science/article/pii/S0017931005000670.
[6] T.R. Ferguson, M.Z. Bazant, Nonequilibrium thermodynamics of porous electrodes, J. Electrochem. Soc. 159 (12) (2012) A1967–A1985, https://doi.org/10.1149/2.048212jes, http://jes.ecsdl.org/content/159/12/A1967.
[7] T.C. Choy, Effective Medium Theory: Principles and Applications, vol. 165, Oxford University Press, 2015.
[8] L. Shen, Z. Chen, Critical review of the impact of tortuosity on diffusion, Chem. Eng. Sci. 62 (14) (2007) 3748–3755, https://doi.org/10.1016/j.ces.2007.03.041, http://www.sciencedirect.com/science/article/pii/S0009250907003144.
[9] Z. Hashin, S. Shtrikman, A Variational approach to the theory of the effective magnetic permeability of multiphase materials, J. Appl. Phys. 33 (10) (1962) 3125–3131, https://doi.org/10.1063/1.1728579, https://aip.scitation.org/doi/abs/10.1063/1.1728579.
[10] M. Ender, J. Joos, T. Carraro, E. Ivers-Tiffée, Three-dimensional reconstruction of a composite cathode for lithium-ion cells, Electrochem. Commun. 13 (2) (2011) 166–168, https://doi.org/10.1016/j.elecom.2010.12.004, http://www.sciencedirect.com/science/article/pii/S1388248110005163.
[11] M. Ender, J. Joos, T. Carraro, E. Ivers-Tiffée, Quantitative characterization of LiFePO4 cathodes reconstructed by FIB/SEM tomography, J. Electrochem. Soc. 159 (7) (2012) A972–A980, https://doi.org/10.1149/2.033207jes, http://jes.ecsdl.org/content/159/7/A972.
[12] M. Ender, An extended homogenized porous electrode model for lithium-ion cell electrodes, J. Power Sources 282 (2015) 572–580, https://doi.org/10.1016/j.jpowsour.2015.02.098, http://www.sciencedirect.com/science/article/pii/S0378775315003432.
[13] C. Argento, D. Bouvard, Modeling the effective thermal conductivity of random packing of spheres through densification, Int. J. Heat Mass Transf. 39 (7) (1996) 1343–1350, https://doi.org/10.1016/0017-9310(95)00257-X, http://www.sciencedirect.com/science/article/pii/001793109500257X.
[14] L.C.R. Schneider, C.L. Martin, Y. Bultel, D. Bouvard, E. Siebert, Discrete modelling of the electrochemical performance of SOFC electrodes, Electrochim. Acta 52 (1) (2006) 314–324, https://doi.org/10.1016/j.electacta.2006.05.018, http://www.sciencedirect.com/science/article/pii/S0013468606005603.
[15] J. Ott, B. Völker, Y. Gan, R.M. McMeeking, M. Kamlah, A micromechanical model for effective conductivity in granular electrode structures, Acta Mech. Sinica 29 (5) (2013) 682–698, https://doi.org/10.1007/s10409-013-0070-x, http://link.springer.com/article/10.1007/s10409-013-0070-x.
[16] J.K. Ott, Modeling the Microstructural and Micromechanical Influence on Effective Properties of Granular Electrode Structures with regard to Solid Oxide Fuel Cells and Lithium Ion Batteries, PhD Thesis, Karlsruhe 2015, https://doi.org/10.5445/IR/1000049833.
[17] Y. Gan, Thermo-mechanics of pebble beds in fusion blankets, PhD Thesis, Karlsruhe, 2008 https://doi.org/10.5445/IR/200074161, https://publikationen.bibliothek.kit.edu/200074161.
[18] H.W. Zhang, Q. Zhou, H.L. Xing, H. Muhlhaus, A DEM study on the effective thermal conductivity of granular assemblies, Powder Technol. 205 (1) (2011) 172–183, https://doi.org/10.1016/j.powtec.2010.09.008, http://www.sciencedirect.com/science/article/pii/S0032591010004833.
[19] J. Gan, Z. Zhou, A. Yu, Particle scale study of heat transfer in packed and fluidized beds of ellipsoidal particles, Chem. Eng. Sci. 144 (2016) 201–215, https://doi.org/10.1016/j.ces.2016.01.041, http://www.sciencedirect.com/science/article/pii/S0009250916300215.
[20] J. Gan, Z. Zhou, A. Yu, Effect of particle shape and size on effective thermal conductivity of packed beds, Powder Technol. 311 (2017) 157–166, https://doi.org/10.1016/j.powtec.2017.01.024, http://www.sciencedirect.com/science/article/pii/S0032591017300347.
[21] O. Stenzel, O. Pecho, L. Holzer, M. Neumann, V. Schmidt, Predicting effective conductivities based on geometric microstructure characteristics, AICHE J. 62 (5) (2016) 1834–1843, https://doi.org/10.1002/aic.15160, http://onlinelibrary.wiley.com/doi/10.1002/aic.15160/abstract.
[22] J.H. van der Linden, G.A. Narsilio, A. Tordesillas, Machine learning framework for analysis of transport through complex networks in porous, granular media: a focus on permeability, Phys. Rev. E 94 (2) (2016), 022904. https://doi.org/10.1103/PhysRevE.94.022904, http://link.aps.org/doi/10.1103/PhysRevE.94.022904.
[23] X. Huang, Q. Zhou, J. Liu, Y. Zhao, W. Zhou, D. Deng, 3d stochastic modeling, simulation and analysis of effective thermal conductivity in fibrous media, Powder Technol. 320 (2017) 397–404, https://doi.org/10.1016/j.powtec.2017.07.068, http://www.sciencedirect.com/science/article/pii/S0032591017306174.
[24] K. Bahr, Electrical anisotropy and conductivity distribution functions of fractal random networks and of the crust: the scale effect of connectivity, Geophys. J. Int. 130 (3) (1997) 649–660, https://doi.org/10.1111/j.1365-246X.1997.tb01859.xhttps://onlinelibrary.wiley.com/doi/abs/10.1111/j.1365-246X.1997.tb01859.x.
[25] A. Kirkby, G. Heinson, L. Krieger, Relating permeability and electrical resistivity in fractures using random resistor network models, J. Geophys. Res. Solid Earth 121 (3) (2016) 1546–1564, https://doi.org/10.1002/2015JB012541https://agupubs.onlinelibrary.wiley.com/doi/abs/10.1002/2015JB012541.
[26] J.T. Gostick, M.A. Ioannidis, M.W. Fowler, M.D. Pritzker, Pore network modeling of fibrous gas diffusion layers for polymer electrolyte membrane fuel cells, J. Power Sources 173 (1) (2007) 277–290, https://doi.org/10.1016/j.jpowsour.2007.04.059http://www.sciencedirect.com/science/article/pii/S0378775307009056.
[27] J. Cai, W. Wei, X. Hu, D.A. Wood, Electrical conductivity models in saturated porous media: a review, Earth Sci. Rev. 171 (2017) 419–433, https://doi.org/10.1016/j.earscirev.2017.06.013http://www.sciencedirect.com/science/article/pii/S0012825217301472.
[28] H. Frohne, F. Moeller (Eds.), Moeller Grundlagen der Elektrotechnik: mit 182 Beispielen, 22nd editionStudium, Vieweg + Teubner, Wiesbaden, 2011, oCLC: 702642494.
[29] P.A. Cundall, O.D.L. Strack, A discrete numerical model for granular assemblies, Géotechnique 29 (1) (1979) 47–65, https://doi.org/10.1680/geot.1979.29.1.47http://www.icevirtuallibrary.com/doi/abs/10.1680/geot.1979.29.1.47.
[30] J. Hoshen, R. Kopelman, Percolation and cluster distribution. I. Cluster multiple labeling technique and critical concentration algorithm, Phys. Rev. B 14 (8) (1976) 3438–3445, https://doi.org/10.1103/PhysRevB.14.3438http://link.aps.org/doi/10.1103/PhysRevB.14.3438.
[31] A. Al-Futaisi, T.W. Patzek, Extension of Hoshen–Kopelman algorithm to non-lattice environments, Phys. A: Stat. Mech. Appl. 321 (3–4) (2003) 665–678, https://doi.org/10.1016/S0378-4371(02)01586-8, http://www.sciencedirect.com/science/article/pii/S0378437102015868.
[32] T. Metzger, A. Irawan, E. Tsotsas, Remarks on the paper "Extension of Hoshen–Kopelman algorithm to non-lattice environments" by A. Al-Futaisi and T.W. Patzek, Physica A 321 (2003) 665–678, Physica A: Statistical Mechanics and its Applications 363 (2) (2006) 558–560, https://doi.org/10.1016/j.physa.2005.08.026, http://www.sciencedirect.com/science/article/pii/S0378437105008654.
[33] C. Rycroft, Voro++: A Three-Dimensional Voronoi Cell Library in C++, https://escholarship.org/uc/item/8sf4t5x8.
[34] H. Carslaw, J. Jaeger, Conduction of Heat in Solids: Oxford Science Publications, England, Oxford, 1959.
[35] G.K. Batchelor, R. W, O'Brien, thermal or electrical conduction through a granular material , proceedings of the Royal Society of London a: mathematical, Phys. Eng. Sci. 355 (1682) (1977) 313–333, https://doi.org/10.1098/rspa.1977.0100. URL http://rspa.royalsocietypublishing.org/content/355/1682/313.
[36] D. Systemes, Abaqus 6.14 Documentation, Providence, RI: Dassault Systemes, 2014.
[37] Boost, Boost C++ Libraries, http://www.boost.org/ 2018.
[38] O. Devillers, S. Loriot, S. Pion, CGAL Ipelets, CGAL User and Reference Manual, 4th editionCGAL Editorial Board, 2018https://doc.cgal.org/4.13/Manual/packages.html#PkgCGALIpeletsSummary.
[39] W.S. Jodrey, E.M. Tory, Computer simulation of close random packing of equal spheres, Phys. Rev. A 32 (4) (1985) 2347–2351, https://doi.org/10.1103/PhysRevA.32.2347http://link.aps.org/doi/10.1103/PhysRevA.32.2347.
[40] Y. Gan, M. Kamlah, J. Reimann, Computer simulation of packing structure in pebble beds, Fus. Eng. Design 85 (10) (2010) 1782–1787, https://doi.org/10.1016/j.fusengdes.2010.05.042, http://www.sciencedirect.com/science/article/pii/S0920379610002541.
[41] R. Landauer, The electrical resistance of binary metallic mixtures, J. Appl. Phys. 23 (7) (1952) 779–784, https://doi.org/10.1063/1.1702301, https://aip.scitation.org/doi/abs/10.1063/1.1702301.
[42] G. Guennebaud, B. Jacob, others, Eigen v3, http://eigen.tuxfamily.org 2010.